Generation and nature of water-tolerant Lewis acid sites in In x Sn 10– x O y /Al 2 O 3 catalysts as active centers for the green synthesis of methyl lactate from glucose

Zhenxiang Zhao, Jun Yang, Ningkun Xu, Tian Nan, Pingping Wu, Chunzheng Wang, Xiaohua Wang, Peng Bai, Zifeng Yan, Svetlana Mintova

ARTICLE

Generation and nature of water-tolerant Lewis acid sites in $In_xSn_{10-x}O_y/Al_2O_3$ catalyst as active centers for green synthesis of methyl lactate from glucose

Received 00th July 20xx
Accepted 00th July 20xx

DOI: 10.1039/x0xx00000x

www.rsc.org/

Zhenxiang Zhao[a], Jun Yang[a], Ningkun Xu[a], Tian Nan[a], Pingping Wu[a], Chunzheng Wang[a], Xiaohua Wang[b], Peng Bai[a,*], Zifeng Yan[a] and Svetlana Mintova[a,c]

Solid Lewis acid catalysts are commonly used in the synthesis of methyl lactate (MLA). However, water as a solvent, reactant, or by-product adsorbed on the Lewis acid sites (LAS), resulted in the deactivation of the LAS. In this work, highly dispersed In-Sn oxide on the surface of alumina support was prepared using interconnected In_2O_3 and SnO_2. The highly dispersed In-Sn oxides effectively decreased the OH groups of the catalyst leading to the decrease of the residual organics and inhibiting the deleterious effect of water on LAS. Besides, the Sn doping resulted in abundant coordinatively unsaturated sites (CUS) on the catalyst surface. The CUS were further partially hydrolyzed forming new OH groups under the action of water during the MLA synthesis thus leading to an increase of the LAS activity. Therefore, after the Sn doping, more LAS were detected in the presence of water, confirming that the $In_xSn_{10-x}O_y/Al_2O_3$ catalyst had more water-tolerant LAS. Under the synergy of lower hydroxyl density and more water-tolerant LAS, the MLA yield of 57.6 % was achieved on the $In_7Sn_3O_y/Al_2O_3$ catalyst, which is the highest reported for the non-zeolite metal oxide catalysts up to now. This work provided a new strategy for the design of non-zeolite metal oxide catalysts with decreased OH groups, increased CUS and no LAS deactivation in the presence of water.

1. Introduction

Polylactic acid (PLA) is an important degradable plastic component that is beneficial for reducing the use of non-degradable plastics. So the dependence on lactic acid (LA) is increasing.[1] So far, nearly 90% of LA is synthesized by fermentation.[2] However, this production route is inefficient, bearing high separation costs and generating calcium sulphate wastes.[3-6] In the LA synthesis, LA was esterified to obtain methyl lactate (MLA), and the separated MLA was hydrolyzed to obtain pure LA. .[7] Therefore, the direct synthesis of MLA skips previous steps and decreases cost. [8] This makes the MLA synthesis from low-cost glucose and methanol by heterogeneous catalysis important to be considered. Therefore, heterogeneous catalytic approaches have been long recognized as potential alternatives to fermentation.[6]

As a heterogeneous catalyst, the tin containing zeolite Beta (Sn-BEA) has been widely investigated for MLA synthesis from glucose and methanol; the achieved MLA yield reported ranges from 43% to 58%.[9, 10] It is commonly recognized that on Lewis acid sites (LAS) of catalysts such as Sn-BEA, glucose (aldose) is initially isomerised to fructose (ketose), followed by a retro-aldol reaction of fructose forming two trioses. These trioses then convert to methyl lactate through sequential dehydration and methanol addition (Fig. S1).[11] Therefore, LAS are the active centres for the conversion of glucose to MLA. However, water, as a by-product, competes with reactants for adsorption on LAS, thus leading to deactivation of the active sites.[12] Researchers have found that water significantly inhibits the activity of LAS in $Nb_2O_5{\cdot}nH_2O$. Nakajima et al. prevents LAS inactivation by synthesizing ortho-Nb_2O_5, which is due to the fact that Nb^{IV} in ortho-Nb_2O_5 remains stable in water.[13] Therefore, water-tolerant LAS are of great importance for MLA synthesis.[14]

As is widely recognized, the generation of water-tolerant LAS in Sn-BEA can be attributed to two features: (a) The coordinatively unsaturated sites (CUS) bind water to produce LAS with higher activity;[15] and (b) Surface hydrophobization reduces the deleterious effect of water on LAS.[12] On one hand, both closed sites (M-$(OSi)_4$) and open sites (HO-M-$(OSi)_3$) exist in the metal-containing zeolites (Sn-BEA, TS-1).[16, 17] In this reaction, the closed sites bind water and partially hydrolyze to the open site with an increased activity (scheme 1 (a-b)).[15] Thus the generation mechanism of the new LAS is associated with CUS. On the other hand, the Sn-BEA was synthesized with the assistance of F^-, which makes the catalysts more hydrophobic.[18] However, the synthesis time is long,[19] and the F^- causes equipment corrosion and environmental pollution. In

[a] State Key Laboratory of Heavy Oil Processing, CNPC Key laboratory of Catalysis, College of Chemistry and Chemical Engineering, China University of Petroleum (East China), Qingdao 266580, P. R. China.
[b] Petrochemical Research Institute, PetroChina Company Limited, Beijing 100195, China.
[c] Normandie University, ENSICAEN, UNICAEN, CNRS, Laboratoire Catalyse et Spectrochimie, 14000 Caen, France.
Tel: 86-86981856. E-mail: baipeng@upc.edu.cn;

order to solve these problems, the generation of silanol by dealumination of BEA zeolite (deAl-BEA) was found to promote the incorporation of Sn into the framework of the Sn-BEA. However, these methods require vacuum conditions[9] or organic solvents refluxing in an inert atmosphere[20] resulting in difficulties in practical application. More importantly, it was found that deAl-BEA based catalysts are obviously hydrophilic,[15, 21, 22] causing decrease in reactivity under aqueous conditions.[15] Therefore, it is highly desired to develop environmentally friendly catalysts with more CUS and hydrophobic surface.

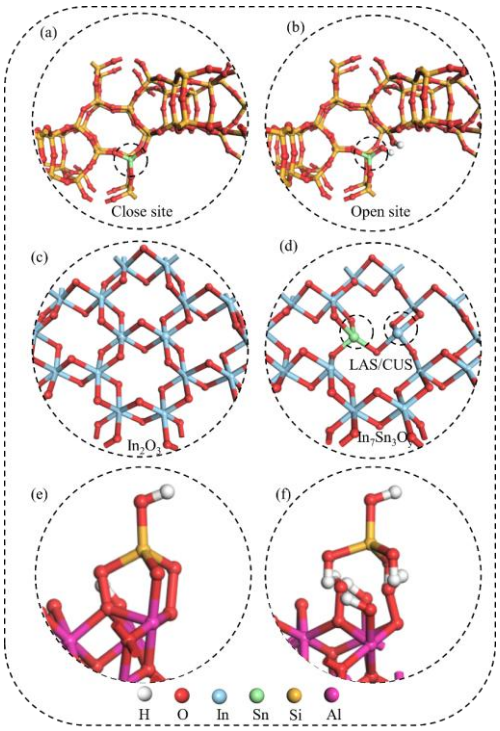

Scheme 1. Structure of the closed site (a) and the open site (b) of Sn-BEA; before and after Sn-doping, construction of CUS or LAS on In_2O_3(222) (c-d); schematic diagram of the interaction between silanol and aluminum hydroxyl on alumina surface (e-f).

Metal oxides such as Al_2O_3, ZrO_2, TiO_2, SnO_2 are environmentally friendly with low costs. These materials are effective in the synthesis of MLA due to their acidic and basic surface sites.[23] As is recognized, hexose sugars (glucose, fructose) or triose sugars (dihydroxyacetone, glyceraldehyde) can be converted to MLA using metal oxide catalysts. Among these metal oxides, Al_2O_3 with highly porous structure exhibits best reactivity in the MLA synthesis. An MLA yield of 34% was achieved when glucose is used as the raw material. However, it has been well recognized that Al_2O_3 with tetrahedrally-coordinated Al^{3+} (Al^{IV}) and octahedrally-coordinated Al^{3+} (Al^{VI}) ions can be rehydrated under hydrothermal conditions to boehmite with only Al^{VI}.[24, 25] As LAS are associated with CUS and this explains why water-tolerant LAS are absent in Al_2O_3. Therefore, it is necessary to hydrophobized the Al_2O_3 surface via reducing the surface OH groups thus to suppress the hydration of the catalyst during MLA synthesis.

It has been reported that metal ions with CUS such as In^{3+}, Nb^{5+} and Ti^{4+} have excellent reactivity.[26-28] And the CUS (Nb^{IV} and Ti^{IV}) were verified to be responsible for the generation of water-tolerant LAS in Nb_2O_5 and TiO_2, indicating that metal oxides with more CUS are conducive to the generation of water-tolerant LAS. As expected, when In_2O_3 was loaded to Al_2O_3, the MLA yield was increased from 21% to 42%.[29] However, the yield is still lower than that of the aforementioned Sn-BEA. This may be due to the low stability of In_2O_3, which sinters seriously during the calcination step. Hence, new approaches are needed to stabilize In_2O_3 and create more CUS in In_2O_3, promoting the formation of water-tolerant LAS.

Since In and Al belong to group IIIA elements, and Sn and Si belong to group IVA elements, similar to aluminum silicate, In and Sn can also form In-Sn oxide (ITO).[30] This material is a necessary component for many modern devices as a traditional transparent electrode, such as touch screens and solar cells.[31] We infer that the interactions between SnO_2 and In_2O_3 may inhibit the sintering of In_2O_3. In addition, as reported before, the silicon doping into alumina increased the concentration of surface CUS (Al^{IV} and Al^{V}), which increases significantly with the increase of silicon.[32] Sn may work similarly as Si leading to an increase of the CUS of In_2O_3/Al_2O_3 (scheme 1 (c-d)).

It should be noted that the under-coordinated ions dispersed on the support may interact with the hydroxyl of the support. Busca has previously described the interaction on the surface of silica-doped alumina (scheme 1 (e-f)).[33] The tetrahedrally-coordinated silicate species tends to maximize the interaction with the alumina by three oxygen atoms, while the fourth oxygen atom forms a hydroxyl group. The formation of Si-O-Al bonds promotes the decrease of OH groups during the synthesis. When three Si-OH of silicate are dehydrated with three Al-OH, three Si-O-Al bonds will form. Considering the fourth Si-OH, the final result is that the three Al-OH disappear and only one Si-OH remains, and 2/3 of the OH groups are decreased. This process has been extended to metal containing zeolite. The Sn precursors dispersed on deAl-BEA generate Sn-O-Si bonds with BEA during vacuum calcination, which reduces the OH groups. These Sn sites are tetrahedrally coordinated.[34] However, it is worth stating that this result cannot be achieved by mechanically mixing SnO_2 with deAl-BEA. This may be attributed to the mechanical mixing difficulties in achieving a uniform dispersion of the Sn species. Unlike Sn^{IV}, the Sn^{VI} in SnO_2 may have more Sn-OH, which is unfavorable for the decrease of OH groups decrease. This is supported by the phenomenon that the changes in OH groups are less when using the wet impregnation of $SnCl_4$. In aqueous solution, during impregnation the possible presence of Sn^{VI} may provide new OH groups. This is not favourable to decrease the OH groups. Therefore, strategies to reduce OH groups may require the uniform dispersion of under-coordinated ions on the support.

In this work, Sn was introduced to In_2O_3/Al_2O_3 to create water-tolerant LAS. This is achieved by suppressing the sintering of In_2O_3 and constructing more CUS after Sn doping. The results show that the dispersion of under-coordinated ions not only reduces OH groups but also provides CUS to form water-tolerant LAS. This allows us to achieve performance enhancement of the $InSnO_x/Al_2O_3$ catalyst by adjusting the In/Sn ratio.

2. Experimental

2.1. Chemicals

Indium nitrate ($In(NO_3)_3$) was purchased from Macklin; stannous chloride dihydrate ($SnCl_2·2H_2O$), ethanol, tin tetrachloride ($SnCl_4$), methanol and D(+)-glucose were purchased from Sinopharm Chemical; acetonitrile-d3 (CD_3CN) and methyl lactate were purchased from Aldrich; pseudo-boehmite was purchased from Shandong Henghui New Material Co., Ltd.

2.2. Preparation of the catalysts

The alumina was obtained by calcining the pseudo-boehmite in a muffle furnace at 550 °C for 2 h and used as a support. The catalysts were prepared using a molar ratio of M/Al=0.1, where M represents In, Sn. The preparation details of all catalysts are shown in Table S1.

In the preparation of a typical catalyst, 2.06 g of $In(NO_3)_3$ was dissolved in 13 mL of ethanol, and 0.66 g of $SnCl_2·2H_2O$ was added to form a sol, followed by the addition of 5 g of alumina and stirred for 2 h. The mixture was dried at 100 °C. The dried solid was calcined in a muffle furnace at 550 °C for 4 h to obtain a catalyst named as $In_xSn_{10-x}O_y/Al_2O_3$.

2.94 g of $In(NO_3)_3$ or 2.21 g of $SnCl_2·2H_2O$ was dissolved in 13 mL of ethanol, followed by the addition of 5 g of alumina and stirred for 2 h. The solid dried at 100 °C was calcined in a muffle furnace at 550 °C for 4 h to obtain catalysts named as In/Al_2O_3 and Sn_{II}/Al_2O_3.

2.3. Characterization

For powder x-ray diffraction (PXRD), all samples were analysed by a Bruker D8 Advance X-ray diffractometer using a nickel filtered Cu *Kα* radiation (*λ*=0.1542 nm). The measurement conditions were set as follows: current of 40 mA, voltage of 35 kV, scanning range of 5 - 75 °, scanning rate of 7 °/min. The diffuse reflectance ultraviolet-visible (diffuse reflectance UV-vis) analysis of the catalyst was performed on a Hitachi U-4100 spectrophotometer using Ba_2SO_4 as the background. Transmission electron microscopy (TEM) and selected area electron diffraction (SAED) images were collected by a JEOL JEM-2100 TEM. Scanning transmission electron microscope-high angle annular dark field (STEM-HAADF) and X-ray energy dispersive spectroscopy (EDS) analyses were conducted with a JEOL JEM-2100F. The porosity of catalysts was analysed by a Quadeasorb evoTM analyser from Anton Paar-Quantachrome. The specific surface area was calculated by the BET (Brunauer-Emmett-Teller) method, the pore size distribution was calculated by the BJH (Barret-Joyner-Halenda) method, and the pore volume was calculated by the adsorption amount corresponding to the highest relative pressure. X-ray photoelectron spectra (XPS) were recorded with an Al *Kα* X-ray spectrometer using a Thermo Fisher Scientific. With the Al electrode as the anode, the electron kinetic energy was 1486.6 eV. The binding energies (BE) were calibrated with C1s BE (284.5 eV) as an internal standard. The thermogravimetric analysis (TGA) was conducted on a NETZSCH STA 449 F5, with which the glucose adsorption capacity of the catalyst was evaluated. In a typical measurement, 0.2 g of the catalyst was placed in 10 mL of glucose aqueous solution (61.7 mM) in water bath at 25 °C for 10 h. Then the solid was filtered and dried at 100 °C. The samples M/Al_2O_3 after adsorption of glucose was denoted as $Glu\text{-}M/Al_2O_3$. The test was carried out in an air atmosphere with the air flow rate of 50 mL/min and the heating rate of 10 °C/min. The amount of adsorbed glucose was calculated by the following equation:

$$Q_1 = \frac{m_2 - m_1}{M}$$

Q_1: glucose adsorption capacity, mmol/g; m_1: catalyst weight loss without glucose adsorption, %; m_2: catalyst weight loss after adsorbing glucose, %; M: molecular weight of glucose.

The acid properties of catalysts were analyzed by the AutoChem II 2920 chemical adsorption instrument produced by Micromeritics. Before the test, the samples were pressed and sieved to 20 ~ 60 mesh. During the test, the temperature was increased to remove impurities in flowing He, and then the gas flow was switched to ammonia after the temperature decreased to 100 °C. After the adsorption was completed, the temperature was increased to 700 °C with a ramping rate of 10 °C/min, and the signal during the desorption process was recorded. The *in situ* transmission FT-IR spectra were collected on a Bruker VERTEX 70V spectrometer. About 10 mg of the catalyst was compressed into a self-supporting pellet with a diameter of 13 mm. The IR spectra of the OH groups of the samples were test in vacuum. The self-supported pellets were treated in vacuum at 500 °C for 1 h. The spectra were collected after cooling to room temperature. For the adsorption of CD_3CN or pyridine (Py-FT-IR), the self-supporting pellet was dehydrated at 500 °C for 1 h and then cooled to room temperature to collect the background. The adsorption was conducted at room temperature, and then the temperature was increased gradually to 100 °C or 150 °C and the spectra were recorded during the heating. In the measurement of glucose conversion, the background was collected without the self-supporting pellet. Then a drop of glucose-methanol solution with a concentration of less than 0.1 mg/g was dropped on the self-supporting pellet. After vacuum evaporation of solvent, the temperature was raised and the spectrum was collected.

Density Functional Theory (DFT) calculations were performed on the Cambridge Sequential DMol^3 of the Materials Studio 8.0. In the process of geometry optimization, the generalized gradient approximation (GGA) was employed with the Perdew Burke Ernzerhof (PBE) exchange correlation functional. We adopted (1×1) unit cells for In_2O_3 (222). The molecular adsorption energies and main reaction energy barriers before and after the isomorphic substitution of Sn on In_2O_3 were compared. The adsorption energy was calculated using the following formula：

$$E_{ads} = E_{adsorbate/surface} - E_{adsorbate} - E_{surface}$$

E_{ads}: adsorption energy; $E_{adsorbate/surface}$: the energy after adsorption of molecules on the surface; $E_{adsorbate}$: the energy of Glucose; $E_{surface}$: the energy of surface.

2.4. Catalytic conversion of glucose to MLA

A 100 mL autoclave was used as the reactor. In a typical reaction run, 0.33 g of glucose was dissolved in 30 mL of methanol, and 0.6 g

of catalyst was added to the mixture. A high-purity nitrogen flow was purged to replace oxygen in the reactor. The temperature of the reactor was raised to 160 °C with stirring and kept for 10 h. After the reaction, the reactor was cooled using a cold water. The catalyst and reaction products were separated by centrifugation. The yield of methyl lactate was measured by a gas chromatograph (GC) equipped with a flame ionization detector (FID) and a HP-5 column. The glucose content in the liquid product was measured by the oxidase electrode method, and the remaining glucose contents for all runs were below the detection limit (< 0.1 mM) with a glucose conversion above 99.84 %. Therefore, only the MLA yield of the catalyst was discussed. The yield of MLA was calculated by the follow formula:

$$\text{Yield} = \frac{\text{Actual moles of methyl lactate produced}}{\text{Theoretical moles of methyl lactate expected}} \times 100\%$$

After the reaction, the catalyst was washed with methanol for three times. The solid was dried, and the residual organics was measured by TGA. The used M/Al_2O_3 catalyst after reaction was denoted as $R\text{-}M/Al_2O_3$. The residual organics was calculated following the formula:

$$\text{Residual organics} = m_3\text{-}m_1$$

Residual organics, %; m_1: catalyst weight loss before the reaction, %; m_3: catalyst weight loss after the reaction, %.

The dried catalyst was calcined in a muffle furnace at 550 °C for 4 h prior to the subsequent reactions cycle.

3. Results and discussion

3.1 Catalyst characterization

PXRD patterns of catalysts are shown in Fig. 1a. The PXRD pattern of the In/Al_2O_3 catalyst contains the characteristic peaks of In_2O_3, indicating the presence of crystalline In_2O_3 particles in this sample. For $In_xSn_{10-x}O_y/Al_2O_3$, the characteristic peaks attributable to In_2O_3 gradually disappear with decreasing the In/Sn ratio, and the PXRD pattern of sample $In_7Sn_3O_y/Al_2O_3$ only contains the characteristic peak of $\gamma\text{-}Al_2O_3$, which may be attributed to the decrease in oxide particle size or to the presence of amorphous particles. Further increasing the doping amount of Sn, the characteristic peaks of SnO_2 appear with the intensity gradually enhanced, and no characteristic peaks attributed to In_2O_3 are detected. This implies that with In/Sn below 7/3, the excessive doping with Sn results in the agglomeration of SnO_2.

Studies have shown that the decrease in metal oxide particle size will result in a decrease in absorbance.[35] Therefore, UV-vis was used to determine the reason for the variation of diffraction peaks in PXRD. The diffuse reflectance UV-vis spectra shown in (Fig. 1b) for samples In/Al_2O_3 and Sn_{II}/Al_2O_3 reveal the absorption attributed to the $O^{2-}\rightarrow In^{3+}$ or $O^{2-}\rightarrow Sn^{4+}$ electronic transition. After doping with Sn, the peaks intensity of In_2O_3 in UV-vis spectra gradually decreases. When the In/Sn ratio is below 7/3, the absorbance intensity exhibits an increasing trend (264-280 nm), which may be attributed to $O^{2-}\rightarrow Sn^{4+}$ electronic transition. This suggests that the lack of signals for sample $In_7Sn_3O_y/Al_2O_3$ in the PXRD is attributed to the decrease in oxide particle size. However, when In/Sn ratio is too high, SnO_2 is sintered on the surface in $In_5Sn_5O_y/Al_2O_3$. This caused the increase of the SnO_2 diffraction peak in the PXRD and the increase of absorption peak in the UV-vis. Band gap analysis also can be used to compare the particle size of metal oxides.[36] As has been reported for Sn-BEA zeolite, the band gap will increase from 4.0 eV to above 5.0 eV.[20] ITO is used for conductive glass coating, and its band gap is usually less than 5.0 eV. However, our results show that when the In/Sn in $In_xSn_{10-x}O_y/Al_2O_3$ approaches 7/3, the band gap gradually increases and reaches the maxima of 5.5 eV (Fig. S2). This means that the metal oxide particle size in sample $In_7Sn_3O_y/Al_2O_3$ may be very small either with nanometric or even sub-nanometer size.

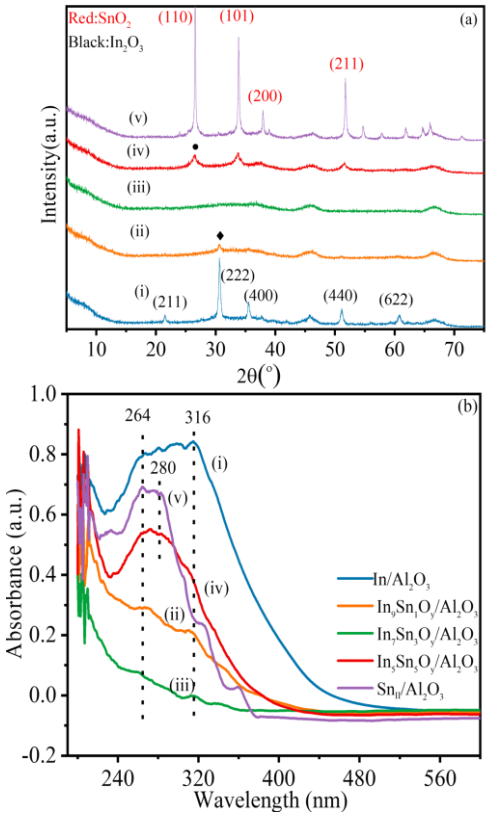

Fig. 1 (a) PXRD patterns and (b) diffuse reflectance UV-vis spectra of catalysts: (i) In/Al_2O_3, (ii) $In_9Sn_1O_y/Al_2O_3$, (iii) $In_7Sn_3O_y/Al_2O_3$, (iv) $In_5Sn_5O_y/Al_2O_3$, (v) Sn_{II}/Al_2O_3.

UV-vis is commonly used to characterize the coordination environment of metal oxide.[37, 38] Since bonding with more OH groups will result in an increase in the coordination number and OH group is an auxochrome, increasing the auxochrome concentration will cause the red shift of absorption peaks.[39] Peaks of Sn-containing materials appear at 210, 230-240, and 280 nm corresponding to Sn species with different coordination environment.[40] The Sn species with lower coordination numbers give rise to absorption peak at lower wavelengths. The peak near 210 nm corresponds to Sn^{IV}, which usually appears in Sn-BEA.[41] The absorption peak at 230–240 nm is attributed to the tin with a coordination greater than four.[20, 42] The peak at 280 nm is attributed to Sn^{VI} of bulk SnO_2. Among all the $In_xSn_{10-x}O_y/Al_2O_3$ samples, the absorption peak for the $In_7Sn_3O_y/Al_2O_3$ exhibited the

largest blue shift (comparison to sample Sn_{II}/Al_2O_3), indicating the highest amount of under-coordinated Sn^{4+}. Similarly, for the indium species, the under-coordinated In species also exhibit absorption at lower wavelengths. And a blue shift of the absorption peak from 316 nm to 281 nm has been observed for indium containing zeolite with BEA type framework structure.[43] As can be seen, compared with sample In/Al_2O_3, among all $In_xSn_{10-x}O_y/Al_2O_3$, the largest blue shift of the absorption peak occurs for the $In_7Sn_3O_y/Al_2O_3$ indicating the highest amount of under-coordinated In^{3+} in sample $In_7Sn_3O_y/Al_2O_3$.

In order to further verify the influence of In/Sn ratio on the size of metal oxide particles, the samples were characterized by TEM. The large particles with a size of 50-100 nm on the In/Al_2O_3 surface can be seen in Fig. S3, and lattice fringes assigned to In_2O_3 crystals are visible in Fig. S4. Dark particles were also detected on the surface of $In_5Sn_5O_y/Al_2O_3$ with a size decreased to 30-50 nm, implying that Sn can inhibit the sintering of In_2O_3 particles. Only a weak halo is observed in the SAED image in Fig.S3 and lattice fringes are assignable to SnO_2 crystalline phase as shown in Fig.S4. This observation is consistent with the weak characteristic peaks for SnO_2 in the PXRD patterns. No obvious In-Sn oxide particles are observed on the surface of sample $In_9Sn_1O_y/Al_2O_3$; very weak electron diffractions are observed in the SAED image, verifying the enhanced dispersion of In-Sn oxide particles on $In_9Sn_1O_y/Al_2O_3$.

The metal oxide particle size and element distribution of sample $In_7Sn_3O_y/Al_2O_3$ were characterized by STEM-HAADF and EDS mapping, respectively. At ordinary STEM observation conditions, only the fibrous morphology of the alumina support can be observed (Fig. 2a). However, in the STEM-HAADF image (Fig. 2b), bright In-Sn oxide particles can be observed due to their higher brightness as compared with Al_2O_3. The In-Sn oxide particles are evenly dispersed on the support with a diameter of less than 10 nm. Fig. 2c demonstrates that the simultaneous presence of In, Sn, Al and O. The line scan results presented as inset in Fig. 2d also show that In and Sn appear at the same time, indicating that there may be electronic interaction between In_2O_3 and SnO_2 that inhibits the aggregation of the two oxide particles on the alumina surface.[44-46]

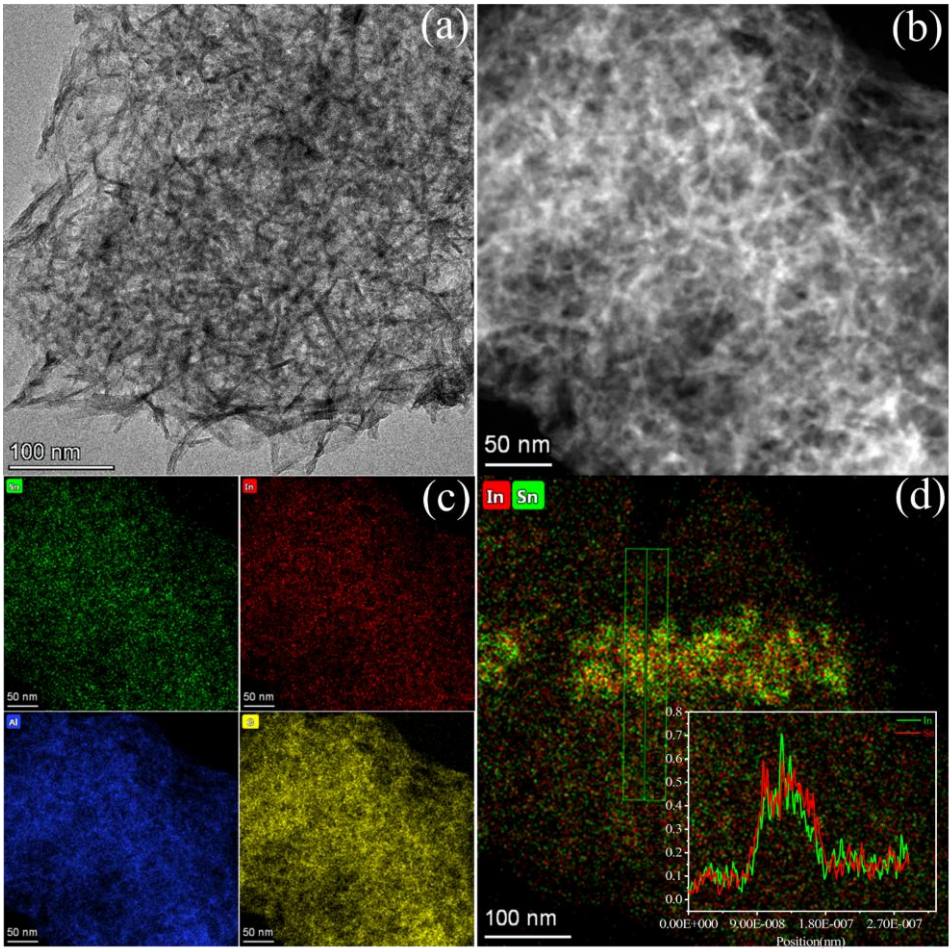

Fig. 2 STEM images (a-b) and EDS mapping (c-d) of $In_7Sn_3O_y/Al_2O_3$. (inset is the energy-dispersive line scan across metal oxide particle using In-L and Sn-L X-rays).

XPS was used to characterize the electronic interactions between In and Sn. The two peaks at 486 and 494 eV are attributed to the $3d_{5/2}$ and $3d_{3/2}$ photoelectrons of Sn species.[47] The two peaks at about 443 eV and 450.3 eV belong to In $3d_{5/2}$ and In $3d_{3/2}$,

respectively (Fig. 3).[43] It can be seen from Fig. 3a that after doping with Sn, the BE of In $3d_{5/2}$ and $3d_{3/2}$ increased by 0.66 eV, suggesting the decrease of electron cloud density.[48] When In is present (Fig. 3b, $In_7Sn_3O_y/Al_2O_3$), the BE of Sn $3d_{5/2}$ and $3d_{3/2}$ decreased by 0.55 eV. This indicates that there is electron transfer from In to Sn in the $In_7Sn_3O_y/Al_2O_3$ sample.

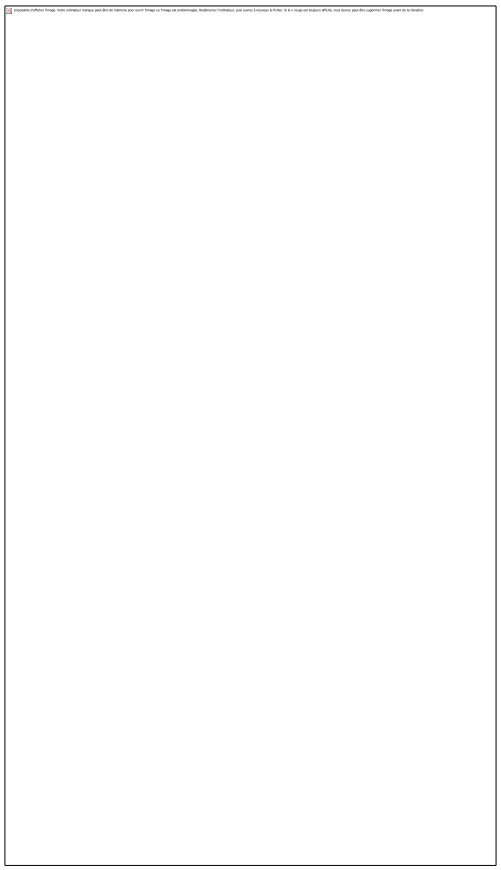

Fig. 3 XPS spectra of In 3d (a) and Sn 3d (b) in In/Al_2O_3, Sn_{II}/Al_2O_3, $In_7Sn_3O_y/Al_2O_3$ catalysts. (Solid black line: baseline; dotted black line: metadata; solid red line: data obtained by fitting; each peak: blue or orange fill.).

The porosity of the samples was evaluated using N_2 adsorption experiments. The results (Fig. S5a) confirmed that both the support and the catalysts exhibit type IV isotherms with obvious hysteresis loops, indicating that all samples have mesoporous structure. The change in the pore size distribution is small (Fig. S5b and Table S2). While the specific surface areas of the catalysts are significantly lower than that of the support (Table S2). Because metal loading is similar, the specific surface areas of all catalysts are similar. However, the pore volume of the catalyst decreased significantly. With the In/Sn ratio approaching 7/3, the pore volume has the lowest value. This may be due to the fact that in the $In_7Sn_3O_y/Al_2O_3$ sample, In-Sn oxides are highly dispersed on the support, which may partially block the mesopores of the support. While in other samples, the In-Sn oxide particles are relatively larger, and are mainly dispersed on the outer surface of the catalyst with less deleterious effect on the pore volume, which has been evidenced by TEM and STEM results.

3.2 Nature and origin of water-tolerant LAS

The catalysts after the glucose adsorption and the reaction were analysed by TGA (Fig. S6). The glucose adsorption capacity and the residual organics were calculated and shown in Table S3. The correlation between the glucose adsorption capacity and MLA yield is presented in Fig. 4a. The margin of error estimated here is based on the standard deviation of three replicate experiments. It can be seen that there is a volcano relationship between glucose adsorption and MLA yield. Too high or too low of glucose adsorption will result in the decreased yield of MLA. Sample $In_7Sn_3O_y/Al_2O_3$ achieved the highest MLA yield of 57.6%. For comparison, the MLA yields in the catalytic conversion of glucose reported previously are summarized in Table S4. The homogeneous catalysts can reach an MLA yield above 60%. For the heterogeneous catalysts, the Sn-BEA achieved the highest MLA yield of 58% ever reported. In contrast, non-zeolite metal oxides catalysts have relatively lower MLA yields, mostly below 40%. Our results demonstrate that the $In_7Sn_3O_y/Al_2O_3$ exhibits the highest MLA yield ever reported for the non-zeolite metal oxide catalysts.

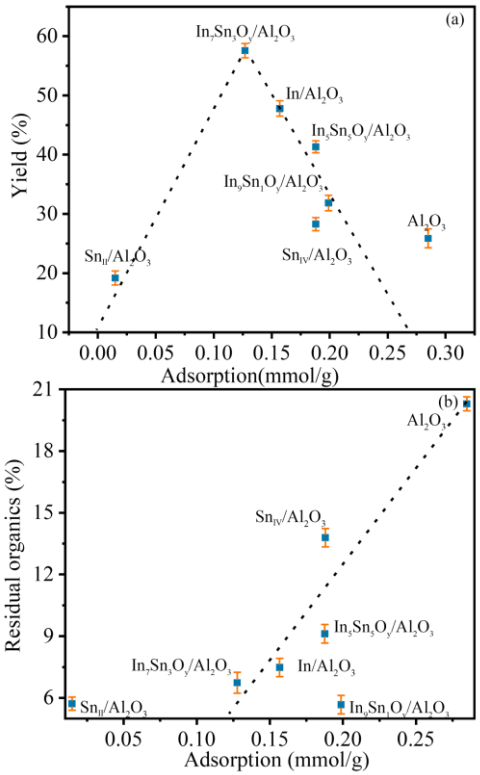

Fig. 4 (a) Relationship between glucose adsorption capacity and MLA yield; (b) glucose adsorption capacity vs. residual organics.

For the catalyst reaction-regeneration cycles, the Al_2O_3 has relatively good performance in this reaction, but the MLA yield decreases significantly during the catalyst reaction-regeneration cycles.[23] This phenomenon is more pronounced for the Al_2O_3 used in this work. By contrast, the $In_7Sn_3O_y/Al_2O_3$ is stable with MLA yield above 50% during three reaction-regeneration cycles (Table S5).

As the In/Sn ratio deviates from 7/3, the glucose adsorption of the catalyst increases, and the yield of MLA decreases. This is attributed to that increasing the glucose adsorption resulted in the conversion of glucose to organic residues (Fig. 4b). Glucose, as a polar molecule, can be adsorbed on both the OH groups and LAS of the catalysts. Hence, in order to explain the differences in the MLA yield and residual organics of catalysts, as shown in Fig. 5, the change in hydroxyl density is followed by *in situ* FT-IR.[34] It is well known that there are multiple OH groups on the surface of alumina. The 3763 cm^{-1} band is with type I_6 OH group (HO-μ_1-Al^{VI}) on the (100) plane, the 3718 cm^{-1} band may be with type I_6 OH group (HO-μ_1-Al^{VI}) on the (111) plane, the 3676 cm^{-1} band is with type I_{66} OH group (HO-μ_2-Al^{VI}) on the (110) and (111) plane.[49] It can be found that these OH groups dominate the alumina surface. The 3740 cm^{-1} band is the tetrahedral $O_3Al(IV)$-OH sites, the 3650 cm^{-1} band is the doubly bridging Al-OH-Al bands.[50] At low temperature dehydration, a spectral band at around 3600 cm^{-1} is attributed to the captured H_2O.[51] There are fewer OH groups in this region which is attributed to the high temperature treatment.

According to Fig. 5, the OH groups of different catalysts can be better attributed to Al-OH, which indicates that the structure of the OH groups has not changed and the hydroxyl density can be semi-quantified based on the mass of alumina. Al_2O_3 has the highest hydroxyl density, which corresponds to its largest glucose adsorption amount and the highest residual organics. After loading indium, the hydroxyl density of the catalyst decreases, so the residual organics is decreased. Among the tested samples, the $In_7Sn_3O_y/Al_2O_3$ possesses the lowest hydroxyl density. After increasing the Sn doping amount, the hydroxyl density of $In_5Sn_5O_y/Al_2O_3$ increases significantly, comparable to that of In/Al_2O_3. Combined with the TEM results, it is clear that the higher hydroxyl density of In/Al_2O_3 and $In_5Sn_5O_y/Al_2O_3$ is attributed to the sintering of oxide particles and the formation of coordinatively saturated sites (UV-vis). Consistent with expectations, the lower hydroxyl density of $In_7Sn_3O_y/Al_2O_3$ is attributed to the uniform dispersion of CUS (from In and Sn) on the alumina surface. The decrease in hydroxyl density is beneficial to lower residual organics, thereby increasing the MLA yield.

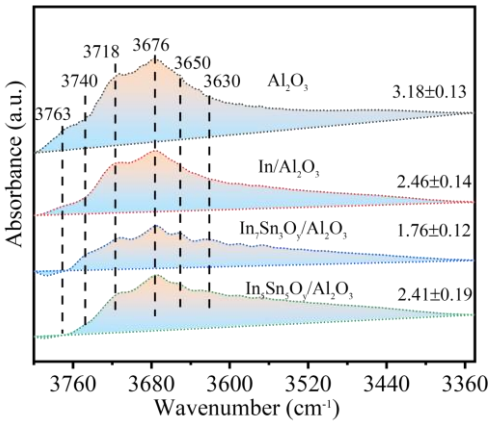

Fig. 5 (a) FT-IR spectra in the OH stretching vibration region of the catalysts (the spectra have been normalized according to the mass of the alumina).

The NH_3-TPD was used to measure the acid amount of catalysts (Fig. S7 and Table S6); the amount of MLA generated per LAS was defined as catalytic efficiency of LAS. It should be noted that normally NH_3-TPD can detect all kinds of acid sites (LAS and Brönsted acid sites), but only LAS was present in the measured catalysts (Fig. 6b). Therefore, here NH_3-TPD measurements provide the amount of LAS. Although $In_7Sn_3O_y/Al_2O_3$ has less LAS than that of In/Al_2O_3, its catalytic efficiency (1.32 h^{-1}) is higher than that of In/Al_2O_3 (0.81 h^{-1}). This may be attributed to the deactivation of the LAS on the In/Al_2O_3 surface in MLA Synthesis. Considering that NH_3-TPD cannot be used to characterize the effect of water on LAS. An attempt was made to characterize the acid amount of the catalyst with water using Py-FT-IR.

In order to verify that $In_7Sn_3O_y/Al_2O_3$ may possess more water-tolerant LAS, the Py-FT-IR characterization was performed on the catalyst saturated with water. As shown in Fig.S8, similar to the previous reports,[13] as the pyridine pressure increases, the peak attributed to water at 1630 cm^{-1} gradually disappears, while the peak of pyridine adsorbed on the catalyst appears at around 1450 cm^{-1}, indicating the competitive adsorption of pyridine and water on the surface. The Py-FT-IR spectra of samples after the physically adsorbed pyridine was removed are shown in Fig. S9. The amounts of LAS are shown in Fig. 6a. The margin of error estimated here is based on the standard deviation of three replicate experiments. It can be seen that the $In_xSn_{10-x}O_y/Al_2O_3$ catalysts exhibit much higher amounts of LAS than those of the monometallic In/Al_2O_3, Sn_{II}/Al_2O_3 and Al_2O_3 samples. After increasing the Sn doping amount, the acid amount first increases and then decreases; the $In_7Sn_3O_y/Al_2O_3$ has the highest

LAS amount. As the amount of LAS was measured under water-saturated conditions, the LAS therefore can be considered as the water-tolerant LAS. These results clearly demonstrate that the $In_7Sn_3O_y/Al_2O_3$ catalyst possesses the highest amount of water-tolerant LAS.

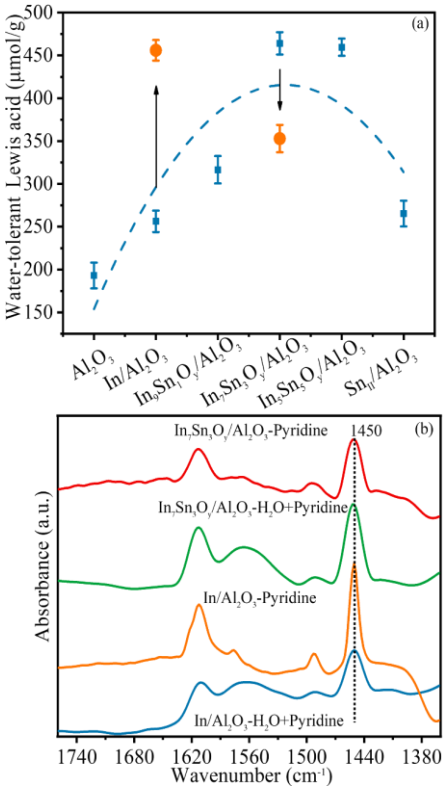

Fig. 6 (a) LAS amount of catalysts (circle symbols: pure pyridine adsorption; cube symbols: pyridine co-adsorbed in the presence of water) and (b) Py-FT-IR spectra of In_7Sn_3Oy/Al_2O_3 and In/Al_2O_3 catalysts with and without water.

The Py-FT-IR spectra of samples In/Al_2O_3 and $In_7Sn_3O_y/Al_2O_3$ with and without water are presented in Fig. 6b. In the presence of water, the intensity of the peak at 1450 cm^{-1} is much lower than that without water for sample In/Al_2O_3. This is also mirrored in Fig. 6a, which shows that although In/Al_2O_3 has a higher content of LAS without water. Considering the severe sintering of In_2O_3 (TEM) and the dominant coordinatively unsaturated In^{3+} on the surface of In/Al_2O_3 (UV-vis), In^{3+} as LAS is less likely. The highest decrease of LAS in the presence of water that can be attributed to that most of the acid sites are provided by alumina. In contrast, the $In_7Sn_3O_y/Al_2O_3$ exhibits a peak with higher intensity near 1450 cm^{-1} in the presence of water than that measured without water, suggesting that water increases the measurable LAS content for sample $In_7Sn_3O_y/Al_2O_3$.

The observed phenomenon is consistent with the previous reports on the open sites of M-containing zeolite.[16, 17] In fact, the similar structure of LAS on alumina surface has also been reported and shown in Fig. S10.[49] Pyridine adsorption on the alumina surface was found to perturb the OH groups. The area of the perturbed OH groups has a good linear relationship with the amount of LAS detected. Therefore, liu et al. [49] concluded that all types of LAS have adjacent OH groups. We believe that these OH groups make the LAS more active and detectable. But we still cannot determine whether the water-tolerant LAS in the $In_7Sn_3O_y/Al_2O_3$ are provided by In or Sn.

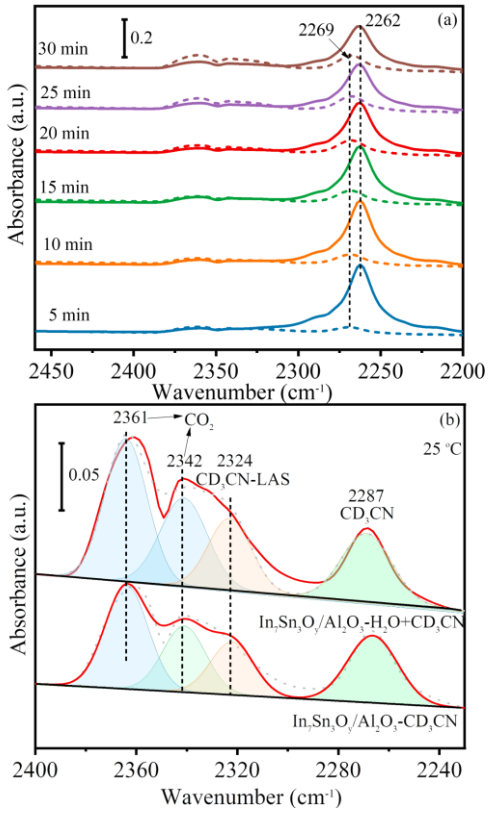

Fig. 7 (a) IR spectra of $In_7Sn_3O_y/Al_2O_3$ using CD_3CN probe molecule with and without water at room temperature (The spectra have been normalized according to the sample mass. Solid line: pure CD_3CN adsorption; Dotted line: CD_3CN co-adsorption with water); (b) IR spectra of $In_7Sn_3O_y/Al_2O_3$ using CD_3CN probe molecule with and without water after desorption at 25 °C (Solid black line: baseline; solid black line: metadata; solid red line: data obtained by fitting; each peak: blue or orange fill.).

In order to identify the origin of water-tolerant LAS in sample $In_7Sn_3O_y/Al_2O_3$, acetonitrile-d3 (CD_3CN) as a probe molecule for LAS,[52] was used to explore the effect of adsorbed water on surface acidity. According to Scheme 1, it can be seen that Sn^{4+} present in Sn-containing zeolites (Sn-BEA) is a typical structure of LAS. The CD_3CN adsorbed to these Sn

sites generated new characteristic peaks in the range of 2316-2308 cm^{-1}.[17, 53, 54] CD_3CN bound to Sn sites in SnO_2 gives rise to a peak at around 2287 cm^{-1},[52] the Sn species on the oxide surface may be similar to Sn-containing zeolite, with open sites detectable near 2320 cm^{-1} and closed sites near 2310 cm^{-1}.[55] A band near 2325 cm^{-1} has been observed assignable to CD_3CN bound to Al^{3+}.[52] Therefore, comparing the effect of water on the CD_3CN adsorption and desorption, we can clarify the origin of water-tolerant LAS. As shown in Fig. 7a, the peaks at 2262 cm^{-1} is attributed to the physically adsorbed CD_3CN, and water decreases the rate and capacity for the CD_3CN adsorption. As shown in Fig. S11, the effect of water on the chemisorption of CD_3CN has been investigated by gradually increasing the temperature in a flowing N_2 atmosphere. A significant weakening of the band of physically adsorbed CD_3CN with increasing temperature has been observed. It should be noted that no evidence of Sn^{4+} as a LAS was observed in the spectra, suggesting that Sn^{4+} on the surface of $In_7Sn_3O_y/Al_2O_3$ is quite different from Sn-BEA or SnO_2, and these Sn^{4+} is less likely to act as a LAS. The bands around 2361 cm^{-1} and 2342 cm^{-1} may be attributed to very small amounts of gas phase or dissolved CO_2. Therefore, it is difficult to distinguish this region of the spectrum. However, we found that the shoulder peak at 2324 cm^{-1} caused a decrease in the symmetry of the spectral band at 2342 cm^{-1}. Considering that this shoulder peak is similar to the LAS of Al^{3+}, we can assume that it contains a band attributed to the influence of LAS. As shown in Fig. 7b, the spectrum obtained after desorption at 25 ^oC was selected for fitting. We can observe that the band near 2324 cm^{-1} is enhanced by the presence of water. Considering the phenomenon that Al_2O_3, In/Al_2O_3, and Sn_{II}/Al_2O_3 have less water-tolerant LAS (Fig. 6a), the water-tolerant LAS of sample $In_7Sn_3O_y/Al_2O_3$ may be derived from the In^{3+} influenced by Sn^{4+} on the basis of excluding sole Sn^{4+} as LAS.

Based on the results presented above, the structure and origin of water-tolerant LAS is proposed and illustrated in Fig. 8. As mentioned earlier, adding Sn enhances the dispersion of In-Sn oxide on support resulting in a decrease of hydroxyl density. Decreasing hydroxyl density leads to decreased influence of water on LAS in MLA synthesis, which is beneficial for increasing of the water-tolerant LAS. However, compared to $In_7Sn_3O_y/Al_2O_3$, although the $In_5Sn_5O_y/Al_2O_3$ possesses a higher content of surface hydroxyl (Fig. 5), it contains a comparable concentration of water-tolerant LAS (Fig. 6a). This indicates that the decrease of hydroxyl density is obviously not the only reason for the generation of water-tolerant LAS, and CUS may be the other factor for the generation of water-tolerant LAS. The (222) crystal plane of In_2O_3 with In^{IV} is presented in Fig. 8. As mentioned earlier, adding Sn increases the under-coordinated ions. In MLA synthesis, decreasing hydroxyl density leads to decreased influence of water, but the under-coordinated ions dispersed on the catalyst surface adsorb water resulting in new OH groups. Under the action of the new OH groups, the acid strength of CUS will increase and become a measurable new LAS. According to the results of UV-vis, it can be seen that the $In_5Sn_5O_y/Al_2O_3$ also possesses under-coordinated In^{3+}, which results in the generation of water-tolerant LAS. It should be mentioned that during the reaction, the amount of CUS decreases due to the binding of hydroxyl by Sn^{IV}, however, this process is reversible. The action of methanol at around 110 ^oC is beneficial for the removal of surface hydroxyl.[56] In fact, hydroxy groups can be effectively removed in the absence of water at around 110 ^oC.[57] And this is lower than the reaction temperature. Therefore, under the action of decreasing surface hydroxyl by methanol, it is possible to realize two cycles: increasing LAS activity by surface bound hydroxyl and reducing hydroxyl to inhibit excessive hydrophilicity, ensuring that there is no excessive loss of CUS (Fig. 8).

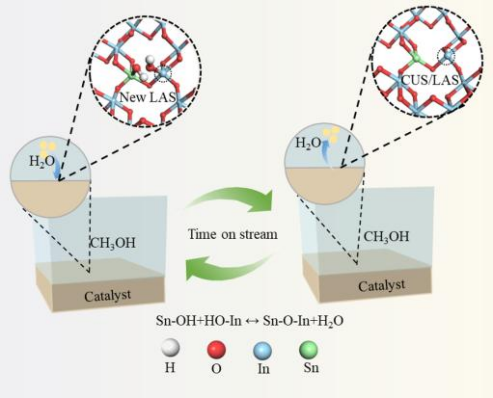

Fig. 8 Structure and origin of water-tolerant LAS: In-Sn oxide with CUS/LAS. The (222) crystal plane of In_2O_3 was selected as the model surface. After doping with Sn, the CUS/LAS were constructed on the surface, and new OH groups were formed on the surface during the reaction. The surface OH groups were decreased by the action of methanol and returned to the original CUS/LAS.

From the previous analysis, it can be seen that lower hydroxyl density and more water-tolerant LAS are important reasons for the superior performance of the $In_7Sn_3O_y/Al_2O_3$ over other supported catalysts. In order to further explain the difference in the performance of catalysts $In_7Sn_3O_y/Al_2O_3$ and In/Al_2O_3 during the reaction process, the *in situ* FT-IR was used to monitor the variation of reaction intermediates and compare with the catalytic results. Since glucose is non-volatile and easy to induce carbon deposition,

it is not possible to contact catalyst via volatilization. Therefore, *in situ* FT-IR studies were rarely conducted for glucose involved reactions. In this work, highly volatile methanol was used as a solvent to dissolve trace amounts of glucose and then dropped onto the self-supporting pellet. Before the test, the system was evacuated at 2 Pa to volatilize the excess of methanol and then the temperature was increased to allow the reaction to happen. As shown in Fig. 9, in both catalysts, new peaks at around 1260, 1450, and 1560 cm^{-1} appeared with increasing the temperature. The peak at 1260 cm^{-1} can be attributed to the enol.[58] For reactions involving carbonyl groups, enol is an important intermediate product.[54] So this peak can be used as indicators of the reaction. As is reported, the peaks around 1450 and 1560 cm^{-1} may belong to the carboxylate species.[58, 59] It is important to note that after the reaction we observed similar bands on the catalyst surface, which facilitated us to attribute them to the target products of the reaction (Fig. S12). As shown, after glucose adsorption, the peak near 1260 cm^{-1} on sample $In_7Sn_3O_y/Al_2O_3$ appears at a lower temperature and increases rapidly in comparison to that for sample In/Al_2O_3. The peaks at 1450 and 1560 cm^{-1} also appear at a relatively lower temperature. This indicates that sample $In_7Sn_3O_y/Al_2O_3$ could transform glucose into enol and then into MLA at a lower temperature, which may be related to higher yield of MLA. This conclusion can also be verified by the difference in MLA yield of the two catalysts at different temperatures as shown in Fig. S13a and b. At different temperatures, the MLA yield of $In_7Sn_3O_y/Al_2O_3$ is also higher than that for In/Al_2O_3.

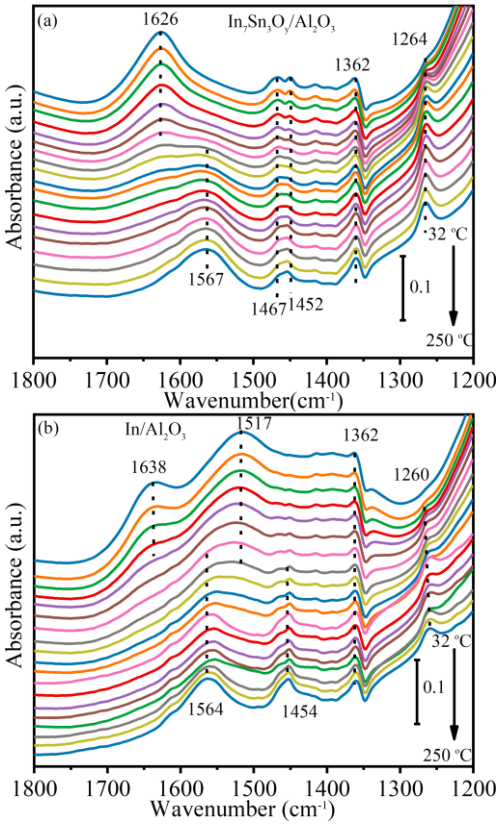

Fig. 9 *In situ* FT-IR spectra of glucose conversion during the heating process on (a) $In_7Sn_3O_y/Al_2O_3$; (b) In/Al_2O_3 catalysts.

To further elucidate the role of Sn addition, the active sites before and after Sn doping were modelled and shown in Fig. 10; methanol was added as a reaction medium. In this model, oxygen terminated In_2O_3 (222) surface was modelled with four-layer slabs, in which the bottom three layers were fixed and the upper one layer and adsorbates were allowed to relax. As shown in Fig. S14, six indium atoms form a period on the surface of In_2O_3(222). The In/Sn ratios in the model can be theoretically set as 1/1, 2/1 or 5/1. In order to combine the experimental results with the model, the measured In/Sn ratio of sample $In_7Sn_3O_y/Al_2O_3$ by EDS and XPS was used. The detection depth of EDS is above 1 μm, and the In/Sn ratio was measured to be 2.10 (close to the theoretical value of 7/3). The detection depth of XPS is 2-5 nm, and the In/Sn ratio measured was 1.62. This indicates that the utmost surface In/Sn ratio is below 1.62, possibly approaching 1/1. The total model height in Fig. S14 is only 8.5 Å, so we set In/Sn ratio of 1/1 for the active surface in $In_7Sn_3O_y/Al_2O_3$.

The adsorption energy of glucose on the surface before and after Sn doping of the catalysts is presented in Fig. 10 and summarized in Table S7. After addition of Sn, glucose is more easily adsorbed

on the active site of the $In_7Sn_3O_y$ catalyst. As mentioned earlier, the decrease of OH groups are not conducive to the adsorption of glucose. The addition of Sn reduces the hydroxyl group but also increases the activity of LAS, which is more conducive to the activation of glucose and provides a basis for the improvement of the MLA yield. As mentioned earlier, enol is an important intermediate in this reaction (Fig. S15 Reaction 1), retro-aldol is the rate-determining step to obtain MLA (Fig. S15 Reaction 2).[3, 54] To this end, we calculated the energy barrier for glucose to form enol and the energy barrier for enol to undergo retro-aldol condensation before and after Sn doping, respectively. The energy barriers for the conversion of glucose to the enol before and after Sn doping of the catalysts are presented in Fig. S16a. The formation energy barrier of the enol is lower after Sn doping. This finding is consistent with the result shown above that glucose is more likely to form the enol at a lower temperature after Sn doping, as evidenced by *in situ* FT-IR of glucose conversion. Fig. S16b compares the energy barriers of enol conversion to glyceraldehyde and dihydroxy acetone, and the reaction energy barrier is significantly decreased after Sn doping, which is consistent with the higher yield of MLA on the $In_7Sn_3O_y/Al_2O_3$ catalyst.

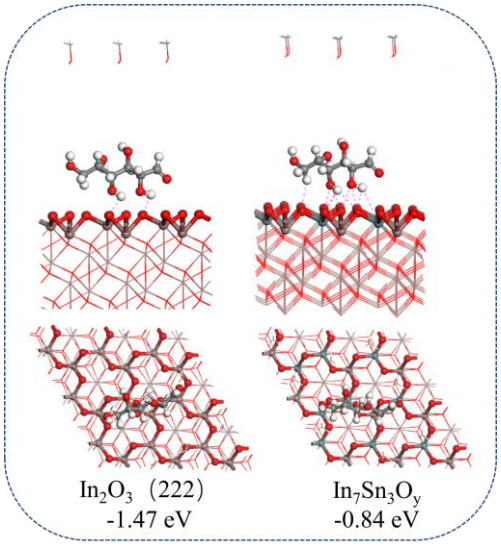

Fig. 10 Adsorption energies of glucose on the In_2O_3 (222) and $In_3Sn_7O_y$ models (eV). (Colour code: red is O, white is H, gray is C, brown is In, and cyan is Sn).

4. Conclusions

This study demonstrates the synthesis of highly dispersed In-Sn oxides on alumina surface, which is beneficial to reduce OH groups and increase CUS to construct water-tolerant LAS. The interactions between SnO_2 and In_2O_3 lead to decrease of metal oxide particle size and form highly dispersed In-Sn oxide on Al_2O_3. Among all tested catalysts, the $In_7Sn_3O_y/Al_2O_3$ possesses the least OH groups and abundant CUS, resulting in the highest amount of water-tolerant LAS. The *in situ* FT-IR results using CD_3CN as LAS probe molecule indicate that the water-tolerant LAS of the $In_7Sn_3O_y/Al_2O_3$ catalyst can be attributed to under-coordinated In^{3+}. In the MLA synthesis, under-coordinated Sn^{4+} is partially hydrolyzed to form new OH groups interacting with under-coordinated In^{3+}, thus enhancing the activity of water-tolerant LAS. Therefore, the $In_7Sn_3O_y/Al_2O_3$ catalyst with the least OH groups and the most water-tolerant LAS exhibited the highest MLA yields (57.58%) among the non-zeolite metal oxide catalysts ever reported for MLA synthesis from glucose and methanol. Theoretical calculations reveal that Sn doping enhanced the adsorption of glucose and decreased the reaction energy barrier of the rate-determining step. These findings shed important light on the design of water-tolerant solid Lewis acid catalysts and provide a new approach to the green synthesis of MLA from glucose.

Conflicts of interest

There are no conflicts to declare.

Acknowledgements

This work was financially supported by Key Projects of China National Key R&D Plan (2022YFA1503400), Natural Science Foundation of China (21991091), Key Projects of Shandong Key R&D plan (2019JZZY010506), Taishan Scholar Foundation (tspd20210308), Petrochina Research and Development Projects (2020A-1816, 2020A-1817) and the Sino-French IRN "Zeolites".

Notes and references

1. M. Morales, P. Y. Dapsens, I. Giovinazzo, J. Witte, C. Mondelli, S. Papadokonstantakis, K. Hungerbühler and J. Pérez-Ramírez, Environmental and economic assessment of lactic acid production from glycerol using cascade bio- and chemocatalysis, *Energy Environ. Sci.*, 2015, **8**, 558-567.

2. D. Verma, R. Insyani, Y.-W. Suh, S. M. Kim, S. K. Kim and J. Kim, Direct conversion of cellulose to high-yield methyl lactate over Ga-doped Zn/H-nanozeolite Y catalysts in supercritical methanol, *Green Chem.*, 2017, **19**, 1969-1982.

3. M. S. Holm, S. Saravanamurugan and E. Taarning, Conversion of Sugars to Lactic Acid Derivatives Using Heterogeneous Zeotype Catalysts, *Science*, 2010, **328**, 602-605.

4. J. Wang, Y. Masui and M. Onaka, Conversion of triose sugars with alcohols to alkyl lactates catalyzed by Bronsted acid tin ion-exchanged montmorillonite, *Appl. Catal. B Environ.*, 2011, **107**, 135-139.

5. P. Mäki-Arvela, I. L. Simakova, T. Salmi and D. Y. Murzin, Production of Lactic Acid/Lactates from Biomass and Their Catalytic Transformations to Commodities, *Chem. Rev.*, 2014, **114**, 1909-1971.

6. M. Dusselier, P. Van Wouwe, A. Dewaele, E. Makshina and B. F. Sels, Lactic acid as a platform chemical in the biobased economy: the role of chemocatalysis, *Energy Environ. Sci.*, 2013, **6**, 1415-1442.

7. R. Alves De Oliveira, M. Alexandri, A. Komesu, J. Venus, C. E. Vaz Rossell and R. Maciel Filho, Current Advances in Separation and Purification of Second-Generation Lactic Acid, *Sep. Purif. Rev.*, 2020, **49**, 159-175.

8. S. P. Kamble, P. P. Barve, J. B. Joshi, I. Rahman and B. D. Kulkarni, Purification of Lactic Acid via Esterification of Lactic Acid Using a Packed Column, Followed by Hydrolysis of Methyl Lactate Using Three Continuously Stirred Tank Reactors (CSTRs) in Series: A Continuous Pilot Plant Study, *Ind. Eng. Chem. Res.*, 2012, **51**, 1506-1514.

9. J. Zhang, L. Wang, G. Wang, F. Chen, J. Zhu, C. Wang, C. Bian, S. Pan and F. S. Xiao, Hierarchical Sn-Beta Zeolite Catalyst for the Conversion of Sugars to Alkyl Lactates, *ACS Sustain. Chem. Eng.*, 2017, **5**, 3123-3131.

10. X. M. Yang, J. J. Bian, J. H. Huang, W. W. Xin, T. L. Lu, C. Chen, Y. L. Su, L. P. Zhou, F. Wang and J. Xu, Fluoride-free and low concentration template synthesis of hierarchical Sn-Beta zeolites: efficient catalysts for conversion of glucose to alkyl lactate, *Green Chem*., 2017, **19**, 692-701.

11. H. Li, Z. Fang, R. L. Smith and S. Yang, Efficient valorization of biomass to biofuels with bifunctional solid catalytic materials, *Prog. Energy Combust. Sci.*, 2016, **55**, 98-194.

12. F. J. Liu, K. Huang, A. M. Zheng, F. S. Xiao and S. Dai, Hydrophobic Solid Acids and Their Catalytic Applications in Green and Sustainable Chemistry, *ACS Catal.*, 2018, **8**, 372-391.

13. K. Nakajima, J. Hirata, M. Kim, N. K. Gupta, T. Murayama, A. Yoshida, N. Hiyoshi, A. Fukuoka and W. Ueda, Facile Formation of Lactic Acid from a Triose Sugar in Water over Niobium Oxide with a Deformed Orthorhombic Phase, *ACS Catal.*, 2018, **8**, 283-290.

14. N. K. Gupta, A. Fukuoka and K. Nakajima, Amorphous Nb_2O_5 as a Selective and Reusable Catalyst for Furfural Production from Xylose in Biphasic Water and Toluene, *ACS Catal.*, 2017, **7**, 2430-2436.

15. P. Wolf, M. Valla, F. Núñez-Zarur, A. Comas-Vives, A. J. Rossini, C. Firth, H. Kallas, A. Lesage, L. Emsley, C. Copéret and I. Hermans, Correlating Synthetic Methods, Morphology, Atomic-Level Structure, and Catalytic Activity of Sn-β Catalysts, *ACS Catal.*, 2016, **6**, 4047-4063.

16. S. Bordiga, F. Bonino, A. Damin and C. Lamberti, Reactivity of Ti(iv) species hosted in TS-1 towards H_2O_2–H_2O solutions investigated by ab initio cluster and periodic approaches combined with experimental XANES and EXAFS data: a review and new highlights, *Phys. Chem. Chem. Phys.*, 2007, **9**, 4854-4878.

17. R. Bermejo-Deval, M. Orazov, R. Gounder, S.-J. Hwang and M. E. Davis, Active Sites in Sn-Beta for Glucose Isomerization to Fructose and Epimerization to Mannose, *ACS Catal.*, 2014, **4**, 2288-2297.

18. H. J. Cho, N. S. Gould, V. Vattipalli, S. Sabnis, W. Chaikittisilp, T. Okubo, B. Xu and W. Fan, Fabrication of hierarchical Lewis acid Sn-BEA with tunable hydrophobicity for cellulosic sugar isomerization, *Microporous Mesoporous Mater.*, 2019, **278**, 387-396.

19. S. Tolborg, A. Katerinopoulou, D. D. Falcone, I. Sádaba, C. M. Osmundsen, R. J. Davis, E. Taarning, P. Fristrup and M. S. Holm, Incorporation of tin affects crystallization, morphology, and crystal composition of Sn-Beta, *J. Mater. Chem. A*, 2014, **2**, 467 - 471.

20. J. C. Vega-Vila, J. W. Harris and R. Gounder, Controlled insertion of tin atoms into zeolite framework vacancies and consequences for glucose isomerization catalysis, *J. Catal.*, 2016, **344**, 108-120.

21. R. Gounder and M. E. Davis, Beyond shape selective catalysis with zeolites: Hydrophobic void spaces in zeolites enable catalysis in liquid water, *AIChE J.*, 2013, **59**, 3349-3358.

22. J. Dijkmans, M. Dusselier, W. Janssens, M. Trekels, A. Vantomme, E. Breynaert, C. Kirschhock and B. F. Sels, An Inner-/Outer-Sphere Stabilized Sn Active Site in β-Zeolite: Spectroscopic Evidence and Kinetic Consequences, *ACS Catal.*, 2016, **6**, 31-46.

23. S. Yamaguchi, M. Yabushita, M. Kim, J. Hirayama, K. Motokura, A. Fukuoka and K. Nakajima, Catalytic Conversion of Biomass-Derived Carbohydrates to Methyl Lactate by Acid–Base Bifunctional γ-Al_2O_3, *ACS Sustain. Chem. Eng.*, 2018, **6**, 8113-8117.

24. Q. Wang, W. Li, I. Hung, F. Mentink-Vigier, X. Wang, G. Qi, X. Wang, Z. Gan, J. Xu and F. Deng, Mapping the oxygen structure of γ-Al_2O_3 by high-field solid-state NMR spectroscopy, *Nat. Commun.*, 2020, **11**, 3620.

25. H.-I. Kim and S. K. Lee, Probing the transformation paths from aluminum (oxy)hydroxides (boehmite, bayerite, and gibbsite) to metastable alumina: A view from high-resolution ^{27}Al MAS NMR, *Am. Mineral.*, 2021, **106**, 389-403.

26. Y. Koito, K. Nakajima, R. Hasegawa, H. Kobayashi, M. Kitano and M. Hara, Lewis acid properties of some metal salts for lactic acid formation in water: ^{31}P NMR spectroscopy with trimethylphosphine oxide as a molecular probe, *Catal. Today*, 2014, **226**, 198-203.

27. K. Nakajima, Y. Baba, R. Noma, M. Kitano, J. N. Kondo, S. Hayashi and M. Hara, $Nb_2O_5{\cdot}nH_2O$ as a heterogeneous catalyst with water-tolerant Lewis acid sites, *J. Am. Chem. Soc.*, 2011, **133**, 4224-4227.

28. K. Nakajima, R. Noma, M. Kitano and M. Hara, Titania as an Early Transition Metal Oxide with a High Density of Lewis Acid Sites Workable in Water, *J. Phys. Chem. C*, 2013, **117**, 16028-16033.

29. Y. Xiao, S. Xu, W. Zhang, J. Li and C. Hu, One-pot chemo-catalytic conversion of glucose to methyl lactate over In/γ-Al_2O_3 catalyst, *Catal. Today*, 2021, **365**, 249-256.

30. M. Davis, K. Zhang, S. Wang and L. J. Hope-Weeks, Enhanced electrical conductivity in mesoporous 3D indium-tin oxide materials, *J. Mater. Chem.*, 2012, **22**, 20163-20165.

31. D. S. Hecht, L. Hu and G. Irvin, Emerging Transparent Electrodes Based on Thin Films of Carbon Nanotubes, Graphene, and Metallic Nanostructures, *Adv. Mater.*, 2011, **23**, 1482-1513.

32. G. Crepeau, V. Montouillout, A. Vimont, L. Mariey, T. Cseri and F. Mauge, Nature, structure and strength of the acidic sites of amorphous silica alumina: An IR and NMR study, *J. Phys. Chem. B*, 2006, **110**, 15172-15185.

33. G. Busca, Catalytic materials based on silica and alumina: Structural features and generation of surface acidity, *Prog. Mater. Sci*, 2019, **104**, 215-249.

34. W. Dai, Q. Lei, G. Wu, N. Guan, M. Hunger and L. Li, Spectroscopic Signature of Lewis Acidic Framework and Extraframework Sn Sites in Beta Zeolites, *ACS Catal.*, 2020, **10**, 14135-14146.

35. Z. Kang, X. Zhang, H. Liu, J. Qiu and K. L. Yeung, A rapid synthesis route for Sn-Beta zeolites by steam-assisted conversion and their catalytic performance in Baeyer–Villiger oxidation, *Chem. Eng. J*, 2013, **218**, 425-432.

36. E. Pighin, V. K. Díez and J. I. Di Cosimo, Synthesis of ethyl lactate from triose sugars on Sn/Al_2O_3 catalysts, *Appl. Catal. A-Gen.*, 2016, **517**, 151-160.

37. J.-K. Yao, K.-R. Fu, Y.-C. Wang, T.-D. Li, H.-X. Liu and J.-G. Wang, Hierarchically porous Sn-β zeolites via an OSDA-free synthesis, *Green Chem.*, 2017, **19**, 3214-3218.

38. R. A. Schoonheydt, UV-VIS-NIR spectroscopy and microscopy of heterogeneous catalysts, *Chem. Soc. Rev.*, 2010, **39**, 5051-5066.

39. X. Qiu, J. Yu, D. Yang, J. Wang, W. Mo and Y. Qian, Whitening Sulfonated Alkali Lignin via H_2O_2/UV Radiation and Its Application As Dye Dispersant, *ACS Sustain. Chem. Eng.*, 2018, **6**, 1055-1060.

40. C.-C. Chang, H. J. Cho, Z. Wang, X. Wang and W. Fan, Fluoride-free synthesis of a Sn-BEA catalyst by dry gel conversion, *Green Chem.*, 2015, **17**, 2943-2951.

41. P. Li, G. Liu, H. Wu, Y. Liu, J. G. Jiang and P. Wu, Postsynthesis and Selective Oxidation Properties of Nanosized Sn-Beta Zeolite, *J. Phys. Chem. C*, 2014, **115**, 3663-3670.

42. R. V. Grieken, C. Martos, M. Sánchez-Sánchez, D. P. Serrano and A. G. Cubero, Synthesis of Sn–silicalite from hydrothermal conversion of SiO_2–SnO_2 xerogels, *Microporous Mesoporous Mater.*, 2009, **119**, 176-185.

43. M. Xia, W. Dong, Z. Shen, S. Xiao, W. Chen, M. Gu and Y. Zhang, Efficient production of lactic acid from biomass-derived carbohydrates under synergistic effects of indium and tin in In-Sn-Beta zeolites, *Sustain. Energy Fuels*, 2020, **4**, 5327-5338.

44. R. T. Hannagan, G. Giannakakis, M. Flytzani-Stephanopoulos and E. C. H. Sykes, Single-

Atom Alloy Catalysis, *Chem. Rev.*, 2020, **120**, 12044-12088.

45. T. Zhang, A. G. Walsh, J. Yu and P. Zhang, Single-atom alloy catalysts: structural analysis, electronic properties and catalytic activities, *Chem. Soc. Rev.*, 2021, **50**, 569-588.

46. R. Lang, X. Du, Y. Huang, X. Jiang, Q. Zhang, Y. Guo, K. Liu, B. Qiao, A. Wang and T. Zhang, Single-Atom Catalysts Based on the Metal–Oxide Interaction, *Chem. Rev.*, 2020, **120**, 11986-12043.

47. Z. Zhu, H. Xu, J. Jiang, Y. Guan and P. Wu, Sn-Beta zeolite hydrothermally synthesized via interzeolite transformation as efficient Lewis acid catalyst, *J. Catal.*, 2017, **352**, 1-12.

48. Q. Sun, B. W. J. Chen, N. Wang, Q. He, A. Chang, C. M. Yang, H. Asakura, T. Tanaka, M. J. Hulsey, C. H. Wang, J. Yu and N. Yan, Zeolite-Encaged Pd-Mn Nanocatalysts for CO_2 Hydrogenation and Formic Acid Dehydrogenation, *Angew Chem. Int. Ed. Engl.*, 2020, **59**, 20183-20191.

49. X. Liu, DRIFTS Study of Surface of γ-Alumina and Its Dehydroxylation, *J. Phys. Chem. C*, 2008, **112**, 5066-5073.

50. K. Khivantsev, N. R. Jaegers, J.-H. Kwak, J. Szanyi and L. Kovarik, Precise Identification and Characterization of Catalytically Active Sites on the Surface of γ-Alumina**, *Angew Chem. Int. Ed. Engl.*, 2021, **60**, 17522-17530.

51. L. Silvester, A. Naim, A. Fateeva, G. Postole, A. Auroux, L. Massin, P. Gelin and L. Bois, Fine tuning of the physico-chemical properties of a MIL-53(Al) type - Mesoporous alumina composite using a facile sacrificial-template synthesis approach, *Microporous Mesoporous Mater.*, 2020, **306**, 110443.

52. J. W. Harris, M. J. Cordon, J. Iorio, J. C. Vega-Vila and R. Gounder, Titration and quantification of open and closed Lewis acid sites in Sn-Beta zeolites that catalyze glucose isomerization, *J. Catal.*, 2016, **335**, 141-154.

53. A. Al-Nayili, K. Yakabi and C. Hammond, Hierarchically porous BEA stannosilicates as unique catalysts for bulky ketone conversion and continuous operation, *J. Mater. Chem. A*, 2016, **4**, 1373-1382.

54. P. Ferrini, J. Dijkmans, R. De Clercq, S. Van de Vyver, M. Dusselier, P. A. Jacobs and B. F. Sels, Lewis acid catalysis on single site Sn centers incorporated into silica hosts, *Coord. Chem. Rev.*, 2017, **343**, 220-255.

55. Q. Hou, M. Zhen, L. Liu, Y. Chen, F. Huang, S. Zhang, W. Li and M. Ju, Tin phosphate as a heterogeneous catalyst for efficient dehydration of glucose into 5-hydroxymethylfurfural in ionic liquid, *Appl. Catal. B Environ.*, 2018, **224**, 183-193.

56. L. Botti, D. Padovan, R. Navar, S. Tolborg, J. S. Martinez-Espin and C. Hammond, Thermal Regeneration of Sn-Containing Silicates and Consequences for Biomass Upgrading: From Regeneration to Preactivation, *ACS Catal.*, 2020, **10**, 11545-11555.

57. D. Padovan, L. Botti and C. Hammond, Active Site Hydration Governs the Stability of Sn-Beta during Continuous Glucose Conversion, *ACS Catal.*, 2018, **8**, 7131-7140.

58. S. Najmi, M. Rasmussen, G. Innocenti, C. Chang, E. Stavitski, S. R. Bare, A. J. Medford, J. W. Medlin and C. Sievers, Pretreatment Effects on the Surface Chemistry of Small Oxygenates on Molybdenum Trioxide, *ACS Catal.*, 2020, **10**, 8187-8200.

59. B. M. Murphy, M. P. Letterio and B. Xu, Catalyst Deactivation in Pyridine-Assisted Selective Dehydration of Methyl Lactate on NaY, *ACS Catal.*, 2017, **7**, 1912-1930.